https://doi.org/10.5194/egusphere-2024-933
Preprint. Discussion started: 2 May 2024

Technical note: Evolution of convective boundary layer height estimated by Ka-band continuous millimeter wave radar at Wuhan in central China

Zirui Zhang[1,2,3] Kaiming Huang[1,2,3] Fan Yi[1,2,3] Fuchao Liu[1,2,3] Jian Zhang[4] and Yue Jia[5]

[1]School of Electronic Information, Wuhan University, Wuhan, China

[2] Key Laboratory of Geospace Environment and Geodesy, Ministry of Education, Wuhan, China

[3]State Observatory for Atmospheric Remote Sensing, Wuhan, China

[4]School of Geophysics and Geomatics, China University of Geosciences, Wuhan, China

[5]NOAA Chemical Sciences Laboratory, Boulder, CO, USA

Email Address: hkm@whu.edu.cn

Zip code: 430072

https://doi.org/10.5194/egusphere-2024-933
Preprint. Discussion started: 2 May 2024

Abstract. Using the vertical velocity (VV) observed by a Ka-band millimeter wave cloud radar (MMCR) at Wuhan, we investigate the evolution of convective boundary layer height (CBLH) based on a specified threshold of VV variance. Compared with the CBLH retrieved from the lidar range corrected signal (RCS), the MMCR-derived CBLH exhibits lower values for a few hours post-sunrise and pre-sunset, but outside these two periods, they are generally in good agreement. Relative to the lidar RCS that is susceptible to the historical aerosol mixing processes, the CBLH estimated from the MMCR VV variance shows a rapid response to thick clouds and a less contamination by aerosol residual layer and long-distance transport of sand and dust, thus the MMCR VV observation can capture the CBLH evolution very well. The MMCR observation in 2020 depicts the seasonal and monthly variations in the CBLH. The seasonal mean CBLH reaches the peak heights of 1.29 km in summer, 1.14 km in spring, and 0.6 km in autumn and winter, with occurrence time between 13:30 and 15:00 LT. The maximum (mean) value of mean (daily maximum) CBLH rises steadily from 0.66 (0.87) km in January to 1.47 (1.76) km July, followed by a gradual decline to 0.42 (0.5) km in December. Statistical standard deviations are monthly-dependent, indicating the significant influence of weather conditions on the CBLH. This study improves our understanding of the Ka-band MMCR's capability to monitor the CBLH, emphasizing its utility in tracking the dynamical processes in the boundary layer.

1. **Introduction**

Atmosphere boundary layer is located in the lowermost layer of the troposphere, and directly impacts the air-land/sea interaction because of its link between the surface and the free atmosphere (Stull, 1988). Owing to the combined effects of gravity, viscosity, and friction of the ground and uneven temperature distribution caused by radiation, the boundary layer is characterized by complex dynamical processes, with the prominent turbulence features of vorticity and compressibility, especially during daytime (Bernardini et al.,

https://doi.org/10.5194/egusphere-2024-933
Preprint. Discussion started: 2 May 2024

2012; Schneider, 2008). Typically, the boundary layer top varies diurnally following the local surface temperature with a magnitude from a few tens of meters to several kilometers. The convective boundary layer (CBL) is a type of atmosphere boundary layer driven primarily by convection. After sunrise, the Earth's surface absorbs solar shortwave radiation, which increases upward sensible heat, enhancing the near-surface convection and elevating the CBL heights (CBLH) gradually (LeMone et al., 2010; Grossman and Robert, 2005; Yates et al., 2001). In the afternoon, as the sensible heat flux decreases, turbulent activity is weakened, causing the CBL to contract downward. Generally, the CBL collapses after sunset, and aerosol particles within the CBL are transformed into a residual layer. The residual layer descends gradually due to the sinking effect until it is mixed with the CBL driven by the next day's post-sunrise convection (Blay-Carreras et al., 2014; Heus et al., 2010; Tennekes and Driedonks, 1981). Since the boundary layer controls the exchanges of heat, momentum, moisture and mass between the ground and the free atmosphere (Mahrt, 1999; Holtslag and Nieuwstadt, 1986), the structure of boundary layer is an important input variable in numerical weather-prediction and climate models (Edwards et al., 2020).

The evolution of CBLH has a distinct daily cycle, which is dominated mainly by surface sensible heat from solar radiation, and can be influenced significantly by weather and local topography (Kwon et al., 2022; Ribeiro et al., 2018). Typically, the CBL is capped by a stable temperature inversion layer, constraining the upward development of convection, thus under the circumstances, the inversion layer bottom is often identified as the top of boundary layer (Stull, 1988). At the height of CBL top, turbulent mixing weakens markedly, leading to substantial changes and strong vertical gradient of atmospheric parameters, such as potential temperature, relative humidity and aerosol concentration. Consequently, the CBL top determines to a great extent the vertical dispersion of aerosol particles (Kong and Yi, 2015; Pal et al., 2015; Stull, 1988). Thus, the CBLH plays a crucial role in air quality and atmospheric environment evaluations, as the concentration of surface emissions and pollutants is closely related to the CBLH (Li et al., 2017; Tang et al.,

https://doi.org/10.5194/egusphere-2024-933
Preprint. Discussion started: 2 May 2024

2016; Liao et al., 2015; Liu and Liang, 2010; Seibert, 2000). Besides, at the boundary top, moisture, aerosols and other chemical substances are entrained to the free atmosphere, creasing an entrainment transition zone between the boundary layer and the free atmosphere (Franck et al., 2021; Liu et al., 2021; Brooks and Fowler, 2007). Hence, the CBLH also plays an important role in influencing the cloud formation and precipitation above the CBL through regulating water vapor and aerosols (as condensation nuclei) entrained into the free atmosphere (Guo et al., 2017; Brooks and Fowler, 2007; Neggers et al., 2004; Brown et al., 2002).

The observations of in situ radiosonde and remote sensing are extensively used to estimate the CBLH and its seasonal feature in different geographical environments. The radiosonde data have a widely geographical distribution and long-term accumulation, which is convenient to study the climatology of boundary layer in different regions. Meanwhile, radiosonde can obtain many meteorological parameters with high precision, such as pressure, temperature, relative humidity, and horizontal wind velocity and direction, providing a possibility to retrieve the boundary layer height through different algorithms (Seidel et al., 2010; Seibert, 2000). Typically, the vertical gradients of potential temperature and water vapor (including relative humidity and specific humidity) are used to determine the CBLH (Zhang et al., 2022; Guo et al., 2021; Dang et al., 2019; Liu and Liang, 2010; Seidel et al., 2010; Stull, 1988). Additionally, the boundary top can be evaluated using the profiles of refractivity and bulk Richardson number derived from the temperature, pressure, vapor pressure and horizontal wind data (Burgos-Cuevas et al., 2021; Guo et al., 2016; Zhang et al., 2014; Seidel et al., 2012; Basha and Ratnam, 2009). These retrieval algorithms provide insights into the features of boundary layer from the perspective of energy exchange, mass transport, turbulent motion and effect on radio propagation. Even so, radiosonde faces a severe limitation to capture the clear development of CBL due to its conventional release schedule, which typically occurs only twice a day.

In contrast to radiosonde, ground-based remote sensing offers high temporal resolution in observational profiles, which is essential to investigate the diurnal evolution of boundary layer. Wind profile radar can obtain the atmospheric wind speed and direction by decomposing the Doppler shift of electromagnetic waves backscattered by the vertical inhomogeneity of atmospheric refractive index structure constant due to the gradients in temperature and relative humidity, and the fluctuation of refractive index caused by turbulence (Liu et al., 2020; Singh et al., 2016; Seibert, 2000). In this way, some parameters from the wind profile radar measurement, such as signal-to-noise ratio, Doppler spectral width and refractive index structure constant, are utilized to retrieve the height of boundary layer for every 30-60 min based on their vertical gradients or chosen thresholds (Burgos-Cuevas et al., 2023; Bianco et al., 2022; Solanki et al., 2021; Liu et al., 2020; Allabakash et al., 2017; Sandeep et al., 2014). Nevertheless, previous studies showed that the top of CBL derived from the radar observation may be influenced by strong residual layer and shallow or large entrainment zone (Sandeep et al., 2014; Bianco and Wilczak, 2002).

Lidar is regarded as a powerful detection equipment for capturing boundary layer development due to its high sensitivity to echo signals from various atmospheric components. Its relatively short operating wavelength allows it to receive echoes backscattered not only from aerosol and cloud particles, but also from atmospheric molecules. Nevertheless, since Rayleigh scattering of atmospheric molecules is much weaker than Mie scattering of aerosol particles, the profile of lidar backscatter coefficient or range corrected signal (RCS) from aerosols is extensively used to determine the CBLH by tracing the height of aerosol concentration plunge. Accordingly, many techniques have been developed to identify the extreme value of RCS gradient (Liu et al., 2021; Su et al., 2020; Dang et al., 2019; Yang et al., 2017; Kong and Yi, 2015; Granados-Muñoz et al., 2012). As a simplified low-power lidar, ceilometer is initially designed to measure the height of cloud base, thus similarly, the backscatter profile from the ceilometer observation can be applied to the CBL investigation (Zhang et al., 2022; Schween et al., 2014; Van Der Kamp and McKendry,

https://doi.org/10.5194/egusphere-2024-933
Preprint. Discussion started: 2 May 2024

2010). However, limited by the ability of lasers to penetrate clouds, the CBLH may be contaminated and even misinterpreted by clouds within the boundary layer in the lidar and ceilometer measurements (Schween et al., 2014).

With the advances in atmospheric sounding technology, the vertical velocity from Doppler lidar provides a direct estimation of convectively driven boundary layer, which can reduce the impact of strong aerosol concentration within the residual layer on the retrieved CBLH (Burgos-Cuevas et al., 2023; Dewani et al., 2023; Huang et al., 2017; Schween et al., 2014; Barlow et al., 2011). At the initial stage of CBL formation in the morning and the rapid decline stage of CBL in the afternoon, aerosol particles in the residual layer may cause the CBLH to be overestimated by about several hundred meters. This discrepancy often reflects the historical effect of aerosol mixing rather than the current situation of convectively driven turbulence (Burgos-Cuevas et al., 2023; Schween et al., 2014; Pearson et al., 2010). In the Doppler lidar observation, a specified threshold of vertical velocity variance is used to define the height of CBL top. This method has been validated as reliable by comparison with the measurements from other equipment, and the sensitivity of threshold has been discussed across different sites (de Arruda et al., 2018; Manninen et al., 2018; Schween et al., 2014; Barlow et al., 2011; Pearson et al., 2010). In contrast to lidar with large blind range and limited penetrating cloud capability, microwave cloud radar offers good low altitude coverage and superior performance in cloud penetration. In the cloud observation, there always exist a weak echo layer near the surface, from which the vertical velocity can be retrieved. However, there are few reports on the use of vertical velocity obtained from Doppler cloud radar for the CBL investigations.

In present study, we estimate the CBLH based on the vertical velocity from a Ka-band millimeter wave cloud radar (MMCR) at Wuhan, and analyze the evolving features of CBL in different seasons by using the observational data with high temporal resolution. In section 2, the instruments and their data are briefly described, followed by the methodology in section 3. In section 4, we present four examples of CBLH

https://doi.org/10.5194/egusphere-2024-933
Preprint. Discussion started: 2 May 2024

diurnal evolution in different seasons by comparing the CBL tops identified from the MMCR and lidar measurements, and then investigate the monthly and seasonal characteristics of CBLH over Wuhan in Section 5. Section 6 provides a summary.

2. Instruments and Data

In this study, the CBLH derived from the MMCR observation is compared with that from the lidar measurement. The Ka-band MMCR and lidar are situated at the Atmospheric Remote Sensing Observatory (ARSO) in Wuhan University (30.5°N, 114.4°E). MMCR antenna is positioned 40 m above sea level, which is about 30 m lower than lidar telescope. Wuhan, an inland megacity in central China, is located in the east of Jianghan Plain, with a resident population of over 12 million. The city is dominated by the subtropical monsoon humid climate, which is characterized with by abundant precipitation and four distinct seasons (Guo et al., 2023). Due to heavy traffic and industrial activities, large amounts of aerosols are emitted from the industrialized metropolis. Meanwhile, sandstorms from the northwest often pass through Wuhan, especially in spring. These sandstorms cause the remarkable variation in the spatial distribution and concentration of aerosols. Frequent sand and dust activity along with cloudy weather poses significant challenges for the Ka-band MMCR and lidar in accurately capturing the CBL evolution.

2.1 Ka-Band Radar

The MMCR established by the ARSO is a Ka-band frequency-modulated continuous wave (FMCW) Doppler radar, which is shown in Figure 1. The radar adopts the mode of transmitting and receiving separation through two same Cassegrain antennas with 1.5 m diameter. Radiation antenna transmits a mean power of 50 W at operating frequency of 35.035 GHz through 0.38° width beam. Backscatter echoes from aerosol and cloud particles are received by reception antenna, and then are sent to the signal processing subsystem to obtain the radial distribution of parameters that represent the characteristics and motion of

https://doi.org/10.5194/egusphere-2024-933
Preprint. Discussion started: 2 May 2024

particles, such as reflectivity factor, Doppler velocity, Doppler spectrum width, signal-to-noise ratio, and so on. Because of almost continuous transmission and reception, FMCW radar has an adjustable range resolution by modulating and demodulating the continuous wave, and a much higher duty cycle relative to pulse radar, leading to a higher temporal resolution in the FMCW radar measurement. In non-precipitation, the MMCR measurement has a time resolution of 0.26 s and a maximum unambiguous velocity of 4.30 m s^{-1}, which are adjusted to be 0.104 s and 10.75 m s^{-1} in precipitation as the size and falling speed of hydrometeors increase (Mao et al., 2023), respectively. The MMCR observation has been applied to the investigations of cloud and precipitation over Wuhan in previous works (Fang et al., 2023; Mao et al., 2023).

The MMCR has a maximum detectable distance of about 30 km and a sensitivity of -30 dBZ at the distance of 10 km. In the MMCR measurement, there are weak echoes generally less than -40 dBz within a few kilometers above the surface. The weak echoes near the surface are attributed to the backscattering of plankton and insects in some studies (Franck et al., 2021; Chandra et al., 2010; Achtemeier, 1991), and are also suggested to come from the scattering of dust particles in other studies (Görsdorf et al., 2015; Clothiaux et al, 2000; Moran et al., 1998). Considering that the size of large dust particles, plant aerosol particles, aerosol particles from combustion, and so on, can be much larger than 10 μm, it is possible for the large aerosol particles to cause these weak echoes in the MMCR observation. The servo-mechanical subsystem conducts the radar to work at specified directional mode or scanning mode. In 2020, the radar was operated at the vertically pointing mode, and the observation is recorded with a vertical resolution of 30 m. In this study, we attempt to explore the CBL evolution at Wuhan from the Ka-band MMCR observation in 2020.

2.2 Polarization Lidar

The polarization lidar developed by the ARSO is about 0.5 km away from the Ka-band radar. The lidar transmits vertically the pulses of 120 mJ at operating wavelength of 532 nm with a repetition rate of 20 Hz by a frequency-doubled Nd: YAG laser. The output polarized laser beam has a fine polarization purity with

https://doi.org/10.5194/egusphere-2024-933
Preprint. Discussion started: 2 May 2024

depolarization ratio less than 1:10000 by using a Brewster polarizer. Light backscattered by aerosol and cloud particles and atmospheric molecules is collected by a telescope with 0.3 m diameter. After separated through an interference filter with 0.3 nm bandwidth centered at 532 nm, the elastically backscattered light is incident on a polarization beam splitter prism, and then the two-channel polarized light are focused onto two photomultiplier tubes (PMTs), respectively. The signals from the two PMTs are transferred to a personal computer (PC)-controlled two-channel transient digitizer to obtain the echo signal intensity and volume depolarization ratio through the PC processing. Backscatter coefficient are retrieved based on the backward iteration algorithm under the condition of a given lidar ratio proposed by Fernald and Klett (Fernald, 1984; Klett, 1981), and then the RCS and particle depolarization ratio are derived from the backscatter coefficient and volume depolarization ratio (Freudenthaler et al., 2009; Immler and Schrems, 2003). Expanded laser beam overlaps with the full field of view of receiving telescope at a height of 0.3 km, thus this height is the low limit of lidar detection. The lidar data has a temporal resolution of 1 min, and a same vertical resolution of 30 m as the MMCR data. The lidar configuration and depolarization comparison with the measurement from the cloud-aerosol lidar and infrared pathfinder satellite observation (CALIPSO) were in detail described in early study (Kong and Yi, 2015).

We regard the height of MMCR antenna as a baseline, thus considering that lidar telescope is about 30 m higher than MMCR antenna, the initial height of lidar data is set at 0.33 km. Meanwhile, in the following analysis, we use local time to represent time.

3. Methodology

In view of the CBLH derived from the vertical velocity (VV) in the MMCR observation but from the RCS in the lidar measurement, we use different algorithms to determine the CBLH, respectively.

3.1 Gradient, Variance and Wavelet Transformation Methods

https://doi.org/10.5194/egusphere-2024-933
Preprint. Discussion started: 2 May 2024

In the lidar observation, the gradient (Grd) method is often utilized to investigate the CBLH by identifying the strongest or minimum gradient of RCS since the intensity of backscattered signal is approximately proportional to the aerosol concentration (Kong and Yi, 2015; Lewis et al., 2013; Pal et al., 2010; Emeis et al., 2008). The wavelet covariance transformation (WCT) method, with a chosen Harr wavelet function, estimates the CBL top by investigating the correlation of the RCS variation with a step function (Zhang et al., 2021; Angelini and Gobbi, 2014; Pal et al., 2010; Baars et al., 2008; Brooks, 2003). Essentially, the WCT method can be considered as a smooth enhancement of Grd method, which may be less affected by noise than the Grd method (Davis et al., 2000; Baars et al. al., 2008).

The Grd and WCT methods derive the CBLH from the change of echo signal intensity in the spatial profile, while the variance (Var) method identifies the CBL top based on the variations of echo signal in the temporal domain. The frequent exchange of matter and energy between the boundary layer and the free atmosphere causes the dramatical variation of aerosol concentration on small time scales around the CBL top. In this case, the height where the variance of backscattered signal reaches the maximum value is regarded as the CBLH (Lammert and Bösenberg, 2006; Martucci et al., 2004; Piironen and Eloranta, 1995). We estimate the CBLH from the lidar RCS every 30 min by using the three methods, and then the obtained height is marked at the central time of 30 min.

3.2 Threshold Method

The VV variance is representative of the level of turbulent activity, thus a threshold of VV variance is applied to determining the CBLH in the Doppler lidar measurement. The threshold is chosen to be 0.04 m^2 s^{-2} in the regions with weak turbulence (Tucker et al., 2009), 0.3 m^2 s^{-2} in a tropical rainforest (Pearson et al., 2010), and 0.4 m^2 s^{-2} in the region with central European climate (Schween et al., 2014; Träumner et al., 2011), while the thresholds of 0.1 and 0.2 m^2 s^{-2} are selected in the urban landscapes since the retrieved CBLH is not heavily dependent on the given thresholds (Burgos-Cuevas et al., 2023; Huang et al. 2017;

Barlow et al., 2011). Similarly, the threshold method is also used to determine the CBLH from the VV variance in the MMCR measurement, with a same duration of 30 min as the lidar observation.

Figure 2 presents the VV from the Ka-band MMCR observation and RCS (in arbitrary unit) from the lidar measurement on 15 August 2020. By taking observations for 30 min from 11:45 to 12:15, we calculate the mean VV and RCS, and estimate the position of CBL top by means of different algorithms, which are shown in Figure 3. From the lidar RCS, the CBLH is 1.35 km in the Grd and WCT methods, and 1.32 km in the Var method, indicating the consistent results for the three algorithms. In the MMCR observation, the VV variance has a clear downward trend with height increasing, with the values of about 1.36 $m^2 s^{-2}$ from the near ground to 0.15 $m^2 s^{-2}$ at 1.47 km, and then maintains slight fluctuations around the value of 0.15 $m^2 s^{-2}$ to higher altitudes. For a specified threshold of 0.3 $m^2 s^{-2}$, the CBL top is identified at the height of 1.35 km, which is in good agreement with the lidar results. It can be noted from Figures 3d and 3f that the CBLHs in the mean RCS profile are around the position with the most rapid change, while the CBLH retrieved from the MMCR VV variance, representing the convectively driven turbulences, is not related to the vertical variation of mean VV. Hence, the good consistency of CBLH derived from the MMCR and lidar demonstrates that the MMCR VV variance is a fine proxy in the estimation of CBLH.

As shown in Figure 3e, the variance decreases quickly from 0.4 $m^2 s^{-2}$ at 1.29 km to 0.15 $m^2 s^{-2}$ at 1.47 km, indicating that the CBH top at noon is less sensitive to the selected threshold within 0.15-0.4 $m^2 s^{-2}$. Figure 4 depicts the CBLHs on 15 August 2020 at the thresholds from 0.2 to 0.45 $m^2 s^{-2}$. Overall, the CBL top declines with the increasing threshold, nevertheless, the CBLH from 09:30 to 17:30 remains relatively stable with little change at the different thresholds. The discrepancy under these thresholds arises mainly in the initial formation and final dissipation stages of CBL due to the large variabilities of turbulences with time and space. Even so, the CBL has an approximately same initial (final) height of about 0.09 (0.12) km at 06:00 (21:00). In following analysis, we take 0.3 $m^2 s^{-2}$ as the threshold to determine the CBLH in the

https://doi.org/10.5194/egusphere-2024-933
Preprint. Discussion started: 2 May 2024

MMCR observation.

4. Case Investigation and Comparison

Figure 5 presents the CBLH evolution on 15 August 2020 from the lidar RCS based on the Grd, Var and WCT methods, and their comparison with that obtained from the MMCR VV variance, together with the distribution of MMCR reflectivity factor in the range of 10-15 km. As shown in Figure 5c, due to the influence of aerosol residual layer, the CBLH from the lidar RCS fluctuates from about 1.56 km at 06:00 down to 1.17 km at 09:30, however, with the sunrise at 05:50, the CBL top derived from the MMCR VV variance gradually rises from about 0.09 km at 06:00 to 1.17 km at 09:30. It is interesting that the CBLH from the lidar RCS variance drops at 07:30, and then shows a change similar to that from the MMCR VV variance. When the CBL ascends gradually and mixes with the residual layer, the CBLHs in the lidar and MMCR observations are consistent with each other between 09:30 and 17:00, including a slight drop at 12:30 and 14:30 (from the gradient and variance of RCS). The maximum height of CBL is about 1.71 km at 14:00 and 15:00 based on the VV variance and the RCS gradient and variance. One can note from the reflectivity factor distribution in Figure 5b that cirrus clouds occur from 17:00, develop rapidly into the thick clouds at about 11-14.4 km at 17:30, and then dissipate quickly after 17:30. In the MMCR observation, the cirrus appearance makes a large contribution to a clear dip in the CBLH between 17:30 and 18:30, nevertheless, the CBL top has a lift as the clouds dissipates rapidly, indicating that the convectively driven turbulence and CBLH have an immediate response to radiation variation. The influence of clouds on the CBLH is also reported in some earlier studies (Dewani et al., 2023; Bianco et al., 2022; Barlow et al., 2011). The phenomenon of CBLH subsidence also arises in the lidar RCS, especially from the RCS variance, but with a time lag due to the influence of historical mixing process on the aerosol distribution (Burgos-Cuevas et al., 2023; Schween et al., 2014). After the sunset at 19:05, the CBLH retrieved by the VV variance drops quickly to 0.27 km at 20:00 from 1.47 km at 19:00, while the top of aerosol residual layer (or horizontally

https://doi.org/10.5194/egusphere-2024-933
Preprint. Discussion started: 2 May 2024

migrating aerosol layer) identified by the lidar stays at far higher level, in particular, from the RCS gradient and WCT.

Next, we select the observations on 31 January, 12 November, and 19 March 2020 to compare the CBLH evolutions. Figure 6 shows the CBLHs on 31 January derived from the four methods above, which are overlaid on the MMCR VV and its variance and the lidar RCS, respectively. It is very cold in January at Wuhan, and the weather is clear from the MMCR observation on 31 January, with a minimum (maximum) temperature of -5 °C (4 °C) recorded in weather forecast. Owing to the convection inhibited largely by the frigid surface and air, the VV variance shows that the CBLH develops very slowly upward to 0.3 km at 11:30 from 0.12 km at 07:30 as the sun rises at 07:15. Thereafter, the top of CBL climbs quickly to 0.9 km at 13:30, and reaches the maximum height of 0.99 km at 14:30, and during this period, the CBLH from the lidar RCS experiences a similarly rapid uplift, and attains the peaks of 1.2 km at 14:00 from the RCS gradient and variance, and 1.14 km at 14:30 from the RCS WCT. In addition, it can be seen from Figure 6d that all the CBLH is slightly larger from the three RCS algorithms than from the VV variance. This implies that a moderately smaller threshold may be appropriate for the estimation of CBLH in winter with weak turbulence (Burgos-Cuevas et al., 2023; Huang et al., 2017; Tucker et al., 2009). After 14:30, the CBLH from the VV variance descends gradually, and approaches the ground at 17:30 prior to the sunset at 17:57, while at the sunset, the CBL top from the RCS is at 0.8-0.9 km due to the history of mixing processes.

Figure 7 presents the CBLHs determined from the MMCR and lidar observations on 12 November 2020. With the sunset on this day in late autumn, the CBLH identified from the VV variance displays a little fluctuation until 10:30. After then, the CBL is rapidly developed to 0.51 km at 11:30, and mixes fully with the residual layer retrieved from the lidar RCS, thus the CBL tops have an approximately same evolution between the MMCR and lidar observations from 11:30 to 17:30, with the maximum values of about 0.75-0.78 km at 15:00 and 16:00. As the sun goes down at 17:27, the CBL from the VV variance rapidly

https://doi.org/10.5194/egusphere-2024-933
Preprint. Discussion started: 2 May 2024

shrinks close to the ground at 18:00, and aerosol particles left in the air form a residual layer, similar to the two cases above.

Figure 8 depicts the CBLH variations in the MMCR and lidar observations on 19 March 2020, together with the depolarization ratio from the lidar. In spring, sandstorms occur frequently in the northwest of China, and sand and dust with different intensities are often blown to Wuhan. On this day, there is a fine sand and dust layer mostly above 1.8 km, with the depolarization ratios of about 0.08-0.12 in Figure 8c, which can also be noted from the MMCR VV distribution. Meanwhile, another sand and dust layer with the larger depolarization ratios of about 0.14-0.16 passes through Wuhan from about 14:00, and mixes with the lower part of the first sand and dust layer. In this situation, the MMCR observation indicates that the CBL starts to develop gently upward from the sunrise, and the upward trend of CBLH is also presented in the lidar measurement, but at higher altitudes. At 09:30, the CBLH is about 0.48 km in both the MMCR and lidar observations, and then rises steadily to 1.32 km at 16:00 and 16:30, shows a good agreement between the two observations. Subsequently, the CBLH from the VV variance undergoes two rapid declines. One occurs from 1.2 km at 17:00 to 0.51 km at 18:00, which is probably related to the sand and dust deposition besides the diminished radiation in the late afternoon, and the other arises after the sunset. However, because of the effect of sand and dust, the CBLH from the lidar RCS increases slightly from 1.32 km at 16:30 to about 1.38 km at 18:00 and 18:30, and then decreases gradually with time.

The CBLH is identified through the spatial and temporal variation of aerosol concentration from the lidar measurement but through the VV change in the time domain from the MMCR observation. The four examples demonstrate that except for a few hours after the sunrise and before the sunset due to the influence of aerosol residual layer, the CBL tops from the MMCR and lidar observations are in good agreement with each other. The residual layer always causes a higher CBLH estimated by the lidar RCS than by the MMCR VV because the convectively driven turbulence represented by the VV variance is less contaminated by the residual layer. Hence, the MMCR VV observation can capture the CBLH evolution very well under a threshold of VV variance, especially for the boundary layer in the blind range of lidar. In view of the seasonal characteristics of convection, a slightly smaller threshold may be more suitable for the CBLH estimation in winter with weaker turbulence. Owing to that the thermally driven convection is sensitive to solar radiation, the CBL top identified from the VV variance has a swift response to clouds, which is distinguished from the lidar observation due to the RCS affected by the history of aerosol mixing processes.

5. Monthly and Seasonal Mean CBLHs

To reveal the general characteristic of CBLH diurnal evolution in different months and seasons, we calculate the monthly and seasonal mean CBLHs by using the MMCR VV on these days without precipitation in 2020. Routinely, winter covers December, January, and February, and so on. Figure 9 illustrates the averaged CBLHs with the standard deviations superimposed on the mean VV variance in each month and season. As we expect, the mean VV variance is the strongest in summer and the weakest in winter. As the spot of direct sunlight slowly moves northward, the mean variance gradually increases from January to July and August, and then decreases step by step from August to December. Interestingly, the variance is significantly larger in spring than in autumn. These monthly and seasonal features of convectively driven turbulence dominate the evolution of monthly and seasonal mean CBLHs. The maximum height of CBL is 1.29 km at 14:30 and 15:00 in summer, 1.14 km at 13:30 in spring, and about 0.6 km at 13:30 and 14:00 in autumn and at 14:30 in winter. In summer, the CBLH displays a feature of quick descent near twilight, and in autumn, the CBL shows a wider envelope with an earlier development and a later dissipation relative to that in winter though their maximum CBLHs are almost the same.

Figure 10 presents the maximum value of monthly mean CBLH and corresponding occurrence time from January to December. The maximum height rises steadily from 0.66 km in January to 1.47 km July and

https://doi.org/10.5194/egusphere-2024-933
Preprint. Discussion started: 2 May 2024

1.44 km in August, and then drops gradually to the lowest altitude of 0.42 km in December. In weather forecast record, there are 7, 3, 13, 3 and 0 days with moderate to heavy rain at Wuhan in September from 2018 to 2022, indicating that September 2020 is a rainy month. The MMCR observation also shows frequently moderate to heavy rains for hours in September 2020, which may be responsible for an evident reduction of CBL maximum height from August to September since a large latent heat flux due to the evaporation on the surface can inhibit the development of thermally driven convection to a certain extent (Dewani et al., 2023; Sandeep et al., 2014). The maximum height occurs is between 13:00 in November and December and 17:30 in July. At Wuhan, the plum rain starts in June and prevails in July. As shown in Figure 9, the CBLH in July has the largest standard deviation (between 13:00 and 19:00) and the latest occurrence time of maximum value over the whole year, which is possibly attributable to the cloudy and rainy weather in addition to the strongest radiation. Similarly, the variability of weather conditions may be a major reason why the maximum height arises 1-2 hours earlier in April-June than in March. Nevertheless, with the gradual decline of solar radiation, the occurrence time of maximum height is steadily advanced from 17:30 in July to 13:00 in November and December.

Finally, we calculate the mean values and standard deviations of daily maximum CBLH and its occurrence time in each month, which is presented in Figure 11. Figure 11 illustrates that the monthly mean value of maximum CBLH has a variational trend similar to the maximum values of monthly mean CBLH in Figure 10. The averaged maximum CBLH is raised from 0.87 km in January to 1.76 km July, and then gradually decreases to the lowest altitude of 0.5 km in December, and its largest and smallest standard deviations also arise in July and December, respectively. The occurrence time of averaged maximum CBLH is the earliest at about 12:40 in December and the latest at 15:45 in August, which is slightly distinguished from those in the maximum value of mean CBLH. The standard deviation of occurrence time is obviously large in January, July and September. These results imply that the maximum height and its occurrence time

https://doi.org/10.5194/egusphere-2024-933
Preprint. Discussion started: 2 May 2024

of daily CBL are significantly influenced by the weather conditions besides radiation since the VV variance as a proxy of convectively driven turbulence is sensitive to the weather changes.

6. Summary

In this study, we investigate the diurnal evolution of monthly and seasonal mean CBLH at Wuhan by the VV variance method based on the Ka-band MMCR observation, and compare the CBLH evolution with that by the RCS gradient, variance and wavelet methods from the lidar measurement.

Using the MMCR VV observation on these days without precipitation in 2020, we statistically analyze the monthly and seasonal variations of CBLH. The maximum value of monthly mean CBLH increases steadily from 0.66 km in January to 1.47 km July and 1.44 km in August, and subsequently, decreases gradually to the lowest height of 0.42 km in December. Analogously, the monthly mean value of daily maximum CBLH rises from 0.87 km in January to 1.76 km July, and then gradually drops to the lowest altitude of 0.5 km in December. The occurrence times is between 13:00 in November and December and 17:30 in July for the maximum value of monthly mean CBLH, but between about 12:40 in December and 15:45 in August for the monthly mean value of daily maximum CBLH, respectively. As for the seasonal feature, the seasonal mean CBLH has the maximum heights of 1.29 km at 14:30 and 15:00 in summer, 1.14 km at 13:30 in spring, and 0.6 km at 13:30 and 14:00 in autumn and at 14:30 in winter. These results are similar to those in early studies (Burgos-Cuevas et al., 2021; Guo et al., 2021; Solanki et al., 2021; Tang et al., 2016; Kong and Yi, 2015). Meanwhile, the statistical standard deviations are monthly-dependent, suggesting that the CBLH is not only regulated mainly by the solar radiation, but also affected significantly by the weather conditions, such as clouds through decreasing radiation to the surface, and precipitation through increasing the latent heat flux.

Besides the maximum values, the MMCR VV variance can capture the initial formation and final

https://doi.org/10.5194/egusphere-2024-933
Preprint. Discussion started: 2 May 2024

dissipation stages of CBL very well relative to the lidar RCS. In the ascending and descending phases of CBL, the CBLH from the lidar RCS is higher than from the MMCR VV variance, due to the high blind range of lidar and the strong influence of aerosol residual layer on the lidar RCS. When the CBLH reaches the height of CBL top identified by the lidar RCS, the CBL tops from the MMCR and lidar observations are in good agreement until it is separated from the top of aerosol residual layer left behind in the late afternoon. Additionally, in comparison to the lidar RCS affected by the history of aerosol mixing processes, the CBLH in the MMCR observation shows a rapid response to clouds and a less contamination by the long-range transport of sand and dust, indicating the efficiency of the VV variance method in the estimation of convectively driven boundary layer, similar to in early studies (Dewani et al., 2023; Huang et al., 2017; Barlow et al., 2011).

The case analysis indicates that the CBLH is not very sensitive to the VV variance thresholds of 0.2-0.45 $m^2 s^{-2}$, thus we chose a constant threshold of 0.3 $m^2 s^{-2}$ across all months and seasons. Whereas, the investigation shows that a slightly smaller threshold may be more suitable for the weak convection in winter, thus considering the seasonal and regional, and even weather characteristics of thermally driven convection, the optimal threshold of VV variance in different scenarios require to be discussed carefully in the future. As is known, the Ka-band MMCR is a powerful instrument for observing clouds and weak precipitation, thus the MMCR measurement gives us an opportunity to study in detail the influence of clouds at different heights on the CBLH and the CBLH evolution under different weather conditions.

In this case, the full-time and full-weather MMCR observation with low blind height can obtain the whole evolution of CBLH in many weather conditions, which is helpful for us to gain an insight into the CBL features and also provides the important input variables for weather-prediction and climate models.

https://doi.org/10.5194/egusphere-2024-933
Preprint. Discussion started: 2 May 2024

Code availability. Software code to obtain the results is available upon request from the corresponding author.

Data availability. All data used are available upon request from the corresponding author.

Author contributions. KH and FY conceptualized this study. ZZ and KH completed the analysis and the manuscript. FL, JZ, YJ, and FY discussed the results and finalized the manuscript.

Competing interests. The authors declare that they have no conflict of interest.

Financial support. This work was supported by the National Key Research and Development Program of China (2022YFB3901800 and 2022YFB3901805) and the National Natural Science Foundation of China (42174189).

References

Allabakash, S., Yasodha, P., Bianco, L., Venkatramana Reddy, S., Srinivasulu, P., and Lim, S.: Improved boundary layer height measurement using a fuzzy logic method: Diurnal and seasonal variabilities of the convective boundary layer over a tropical station, J. Geophys. Res.-Atmos., 122, 9211–9232, https://doi.org/10.1002/2017JD027615, 2017.

Achtemeier, G. L.: The use of insects as tracers for “Clear-Air” boundary-layer sturdies by doppler radar, J. Atmos. Ocean. Tech., 8, 746-765, https://doi.org/10.1175/1520-0426(1991)008<0746:TUOIAT>2.0.CO;2, 1991.

Baars, H., Ansmann, A., Engelmann, R., and Althausen, D.: Continuous monitoring of the boundary-layer top with lidar, Atmos. Chem. Phys., https://doi.org/10.5194/acp-8-7281-2008, 2008.

Barlow, J. F., Dunbar, T. M., Nemitz, E. G., Wood, C. R., Gallagher, M. W., Davies, F., O’Connor, E., and Harrison, R. M.: Boundary layer dynamics over London, UK, as observed using Doppler lidar during

https://doi.org/10.5194/egusphere-2024-933
Preprint. Discussion started: 2 May 2024

REPARTEE-II, Atmos. Chem. Phys., 11, 2111–2125, https://doi.org/10.5194/acp-11-2111-2011, 2011.

Basha, G. and Ratnam, M. V.: Identification of atmospheric boundary layer height over a tropical station using high-resolution radiosonde refractivity profiles: Comparison with GPS radio occultation measurements, J. Geophys. Res.-Atmos., 114, 2008JD011692, https://doi.org/10.1029/2008JD011692, 2009.

Bernardini, M., Pirozzoli, S., and Orlandi, P.: Compressibility effects on roughness-induced boundary layer transition, Int. J. Heat Fluid Fl., 35, 45–51, https://doi.org/10.1016/j.ijheatfluidflow.2012.02.007, 2012.

Bianco, L. and Wilczak, J. M.: Convective boundary layer depth: Improved measurement by doppler radar wind profiler using fuzzy logic methods, J. Atmos. Ocean. Tech., 19, 1745–1758, https://doi.org/10.1175/1520-0426(2002)019<1745:CBLDIM>2.0.CO;2, 2002.

Bianco, L., Muradyan, P., Djalalova, I., Wilczak, J. M., Olson, J. B., Kenyon, J. S., Kotamarthi, R., Lantz, K., Long, C. N., and Turner, D. D.: Comparison of observations and predictions of daytime planetary-boundary-layer heights and surface meteorological variables in the Columbia river gorge and basin during the second wind forecast improvement project, Bound.-Lay. Meteorol., 182, 147–172, https://doi.org/10.1007/s10546-021-00645-x, 2022.

Blay-Carreras, E., Pino, D., Vilà-Guerau De Arellano, J., Van De Boer, A., De Coster, O., Darbieu, C., Hartogensis, O., Lohou, F., Lothon, M., and Pietersen, H.: Role of the residual layer and large-scale subsidence on the development and evolution of the convective boundary layer, Atmos. Chem. Phys., 14, 4515–4530, https://doi.org/10.5194/acp-14-4515-2014, 2014.

Brooks, I. M.: Finding Boundary Layer Top: Application of a wavelet covariance transform to lidar backscatter profiles, J. Atmos. Ocean. Tech., 20, 1092–1105, https://doi.org/10.1175/1520-0426(2003)020<1092:FBLTAO>2.0.CO;2, 2003.

Brooks, I. M. and Fowler, A. M.: A new measure of entrainment zone structure, Geophys. Res. Lett., 34,

https://doi.org/10.5194/egusphere-2024-933
Preprint. Discussion started: 2 May 2024

2007GL030958, https://doi.org/10.1029/2007GL030958, 2007.

Brown, A. R., Cederwall, R. T., Chlond, A., Duynkerke, P. G., Golaz, J. -C., Khairoutdinov, M., Lewellen, D. C., Lock, A. P., MacVean, M. K., Moeng, C. -H., Neggers, R. A. J., Siebesma, A. P., and Stevens, B.: Large-eddy simulation of the diurnal cycle of shallow cumulus convection over land, Q. J. Roy. Meteor. Soc., 128, 1075–1093, https://doi.org/10.1256/003590002320373210, 2002.

Burgos-Cuevas, A., Adams, D. K., García-Franco, J.L., and Ruiz-Angulo, A.: A seasonal climatology of the Mexico City atmospheric boundary layer, Bound.-Lay. Meteorol., 180, 131–154, https://doi.org/10.1007/s10546-021-00615-3, 2021.

Burgos-Cuevas, A., Magaldi, A., Adams, D. K., Grutter, M., García-Franco, J. L., and Ruiz-Angulo, A.: Boundary layer height characteristics in Mexico City from two remote sensing techniques, Bound.-Lay. Meteorol., 186, 287–304, https://doi.org/10.1007/s10546-022-00759-w, 2023.

Chandra, A. S., Kollias, P., Giangrande, S. E., and Klein, S. A.: Long-term observations of the convective boundary layer using insect radar returns at the SGP ARM climate research facility, J. Climate, 23, 5699–5714, https://doi.org/10.1175/2010JCLI3395.1, 2010.

Clothiaux, E. E., Ackerman, T. P., Mace, G. G., Moran, K. P., Marchand, R. T., Miller, M. A., and Martner, B. E.: Objective determination of cloud heights and radar reflectivities using a combination of active remote sensors at the ARM CART sites, J. Appl. Meteorol., 39, 645–665, https://doi.org/10.1175/1520-0450(2000)039<0645:ODOCHA>2.0.CO;2, 2000.

Dang, R., Yang, Y., Hu, X.-M., Wang, Z., and Zhang, S.: A review of techniques for diagnosing the atmospheric boundary layer height (ABLH) using aerosol lidar data, Remote Sens.-Basel, 11, 1590, https://doi.org/10.3390/rs11131590, 2019.

Davis, K. J., N. Gamage, C. Hagelberg, C. Kiemle, D. Lenschow, and P. Sullivan: An objective method for deriving atmospheric structure from airborne lidar observations, J. Atmos. Ocean. Tech., 17, 1455–1468, doi:10.1175/1520-0426(2000)017<1455:AOMFDA>2.0.CO;2, 2000.

de Arruda Moreira, G., Guerrero-Rascado, J. L., Bravo-Aranda, J. A., Benavent-Oltra, J. A., Ortiz-Amezcua, P., Román, R., Bedoya-Velásquez, A. E., Landulfo, E., and Alados-Arboledas, L.: Study of the planetary boundary layer by microwave radiometer, elastic lidar and Doppler lidar estimations in Southern Iberian Peninsula, Atmos. Res., 213, 185–195, https://doi.org/10.1016/j.atmosres.2018.06.007, 2018.

Dewani, N., Sakradzija, M., Schlemmer, L., Leinweber, R., and Schmidli, J.: Dependency of vertical velocity variance on meteorological conditions in the convective boundary layer, Atmos. Chem. Phys., 23, 4045–4058, https://doi.org/10.5194/acp-23-4045-2023, 2023.

Edwards, J. M., Beljaars, A. C. M., Holtslag, A. A. M., and Lock, A. P.: Representation of boundary-layer processes in numerical weather prediction and climate models, Bound.-Lay. Meteorol., 177, 511–539, https://doi.org/10.1007/s10546-020-00530-z, 2020.

Emeis, S., K. Schäfer, and C. Münkel: Surface-based remote sensing of the mixing-layer height—A review, Meteorol. Z., 17, 621–630, https://doi.org/10.1127/0941-2948/2008/0312, 2008.

Fang, J., Huang, K., Du, M., Zhang, Z., Cao, R., and Yi, F.: Investigation on cloud vertical structures based on Ka-band cloud radar observations at Wuhan in Central China, Atmos. Res., 281, 106492, https://doi.org/10.1016/j.atmosres.2022.106492, 2023.

Federico Angelini and Gian Paolo Gobbi: Some remarks about lidar data preprocessing and different implementations of the gradient method for determining the aerosol layers, Ann. Geophys.-Italy, 57, 4, https://doi.org/10.4401/ag-6408, 2014.

Fernald, F. G.: Analysis of atmospheric lidar observations: Some comments, Appl. Opt., 23, 652–653, https://doi.org/10.1364/AO.23.000652, 1984.

Franck, A., Moisseev, D., Vakkari, V., Leskinen, M., Lampilahti, J., Kerminen, V.-M., and O'Connor, E.:

https://doi.org/10.5194/egusphere-2024-933
Preprint. Discussion started: 2 May 2024

Evaluation of convective boundary layer height estimates using radars operating at different frequency bands, Atmos. Meas. Tech., 14, 7341–7353, https://doi.org/10.5194/amt-14-7341-2021, 2021.

Freudenthaler, V., Esselborn, M., Wiegner, M., Heese, B., Tesche, M., Ansmann, A., Müller, D., Althausen, D., Wirth, M., Fix, A., Ehret, G., Knippertz, P., Toledano, C., Gasteiger, J., Garhammer, M., and Seefeldner, M.: Depolarization ratio profiling at several wavelengths in pure Saharan dust during SAMUM 2006, Tellus B, 61, 165, https://doi.org/10.1111/j.1600-0889.2008.00396.x, 2009.

Görsdorf, U., Lehmann, V., Bauer-Pfundstein, M., Peters, G., Vavriv, D., Vinogradov, V., and Volkov, V.: A 35-GHz polarimetric doppler radar for long-term observations of cloud parameters—description of system and data processing, J. Atmos. Ocean. Tech., 32, 675–690, https://doi.org/10.1175/JTECH-D-14-00066.1, 2015.

Granados-Muñoz, M. J., Navas-Guzmán, F., Bravo-Aranda, J. A., Guerrero-Rascado, J. L., Lyamani, H., Fernández-Gálvez, J., and Alados-Arboledas, L.: Automatic determination of the planetary boundary layer height using lidar: One-year analysis over southeastern Spain, J. Geophys. Res.-Atmos., 117, https://doi.org/10.1029/2012JD017524, 2012.

Grossman and Robert, L.: Observed effects of horizontal radiative surface temperature variations on the atmosphere over a midwest watershed during CASES 97, J. Geophys. Res.-Atmos., 110, https://doi.org/10.1029/2004JD004542, 2005.

Guo, J., Miao, Y., Zhang, Y., Liu, H., Li, Z., Zhang,W., He, J., Lou, M., Yan, Y., Bian, L., and Zhai, P.: The climatology of planetary boundary layer height in China derived from radiosonde and reanalysis data, Atmos. Chem. Phys., 16, 13309–13319, https://doi.org/10.5194/acp-16-13309-2016, 2016.

Guo, J., Su, T., Li, Z., Miao, Y., Li, J., Liu, H., Xu, H., Cribb, M., and Zhai, P.: Declining frequency of summertime local-scale precipitation over eastern China from 1970 to 2010 and its potential link to aerosols, Geophys. Res. Lett., 44, 5700–5708, https://doi.org/10.1002/2017GL073533, 2017.

https://doi.org/10.5194/egusphere-2024-933
Preprint. Discussion started: 2 May 2024

Guo, J., Zhang, J., Yang, K., Liao, H., Zhang, S., Huang, K., Lv, Y., Shao, J., Yu, T., Tong, B., Li, J., Su, T., Yim, S. H. L., Stoffelen, A., Zhai, P., and Xu, X.: Investigation of near-global daytime boundary layer height using high-resolution radiosondes: first results and comparison with ERA5, MERRA-2, JRA-55, and NCEP-2 reanalyses, Atmos. Chem. Phys., 21, 17079–17097, https://doi.org/10.5194/acp-21-17079-2021, 2021.

Guo, X., Huang, K., Fang, J., Zhang, Z., Cao, R., Yi, F.: Seasonal and diurnal changes of air temperature and water vapor observed with a microwave radiometer in Wuhan, China, Remote Sens.-Basel, 15, 5422. https://doi.org/10.3390/rs15225422, 2023.

Heus, T., Van Heerwaarden, C. C., Jonker, H. J. J., Pier Siebesma, A., Axelsen, S., Van Den Dries, K., Geoffroy, O., Moene, A. F., Pino, D., De Roode, S. R., and Vilà-Guerau De Arellano, J.: Formulation of the Dutch Atmospheric Large-Eddy Simulation (DALES) and overview of its applications, Geosci. Model Dev., 3, 415–444, https://doi.org/10.5194/gmd-3-415-2010, 2010.

Holtslag, A. A. M. and Nieuwstadt, F. T. M.: Scaling the atmospheric boundary layer, Bound.-Lay. Meteorol., 36, 201–209, https://doi.org/10.1007/BF00117468, 1986.

Huang, M., Gao, Z., Miao, S., Chen, F., LeMone, M. A., Li, J., Hu, F., and Wang, L.: Estimate of boundary-layer depth over Beijing, China, using doppler lidar data during SURF-2015, Bound.-Lay. Meteorol., 162, 503–522, https://doi.org/10.1007/s10546-016-0205-2, 2017.

Immler, F. and Schrems, O.: Vertical profiles, optical and microphysical properties of Saharan dust layers determined by a ship-borne lidar, Atmos. Chem. Phys., https://doi.org/10.5194/acp-3-1353-2003, 2003.

Klett, J. D.: Stable analytical inversion solution for processing lidar returns, Appl. Opt., 20, 211–220, https://doi.org/10.1364/AO.20.000211, 1981.

Kong, W. and Yi, F.: Convective boundary layer evolution from lidar backscatter and its relationship with surface aerosol concentration at a location of a central China megacity, J. Geophys. Res.-Atmos., 120,

https://doi.org/10.5194/egusphere-2024-933
Preprint. Discussion started: 2 May 2024

7928–7940, https://doi.org/10.1002/2015JD023248, 2015.

Kwon, H.-G., Yang, H., and Yi, C.: Study on radiative flux of road resolution during winter based on local weather and topography, Remote Sens.-Basel, 14, 6379, https://doi.org/10.3390/rs14246379, 2022.

Lammert, A. and Bösenberg, J.: Determination of the convective boundary-layer height with laser remote sensing, Bound.-Lay. Meteorol., 119, 159–170, https://doi.org/10.1007/s10546-005-9020-x, 2006.

LeMone, M. A., Chen, F., Tewari, M., Dudhia, J., Geerts, B., Miao, Q., Coulter, R. L., and Grossman, R. L.: Simulating the IHOP_2002 fair-weather CBL with the WRF-ARW–Noah modeling system. Part I: Surface fluxes and CBL structure and evolution along the eastern track, Mon. Weather Rev., 138, 722–744, https://doi.org/10.1175/2009MWR3003.1, 2010.

Lewis, J., E. J. Welton, A. M. Molod, and E. Joseph: Improved boundary layer depth retrievals from MPLNET, J. Geophys. Res.-Atmos., 118, 9870–9879, https://doi.org/10.1002/jgrd.50570, 2013.

Li, H., Yang, Y., Hu, X., Huang, Z., Wang, G., Zhang, B., and Zhang, T.: Evaluation of retrieval methods of daytime convective boundary layer height based on lidar data, J. Geophys. Res.-Atmos., 122, 4578–4593, https://doi.org/10.1002/2016JD025620, 2017.

Liao, J., Wang, T., Jiang, Z., Zhuang, B., Xie, M., Yin, C., Wang, X., Zhu, J., Fu, Y., and Zhang, Y.: WRF/Chem modeling of the impacts of urban expansion on regional climate and air pollutants in Yangtze River Delta, China, Atmos. Environ., 106, 204–214, https://doi.org/10.1016/j.atmosenv.2015.01.059, 2015.

Liu, B., Guo, J., Gong, W., Shi, L., Zhang, Y., and Ma, Y.: Characteristics and performance of wind profiles as observed by the radar wind profiler network of China, Atmos. Meas. Tech., 13, 4589–4600, https://doi.org/10.5194/amt-13-4589-2020, 2020.

Liu, F., Yi, F., Yin, Z., Zhang, Y., He, Y., and Yi, Y.: Measurement report: characteristics of clear-day convective boundary layer and associated entrainment zone as observed by a ground-based polarization lidar over Wuhan (30.5° N, 114.4° E), Atmos. Chem. Phys., 21, 2981–2998, https://doi.org/10.5194/acp-21-2981-2021, 2021.

Liu, S. and Liang, X.-Z.: Observed diurnal cycle climatology of planetary boundary layer height, J. Climate, 23, 5790–5809, https://doi.org/10.1175/2010JCLI3552.1, 2010.

Mahrt, L.: Stratified atmospheric boundary layers, Bound.-Lay. Meteorol., 90, 375–396, https://doi.org/10.1023/A:1001765727956, 1999.

Manninen, A. J., Marke, T., Tuononen, M., and O'Connor, E. J.: Atmospheric boundary layer classification with doppler lidar, J. Geophys. Res.-Atmos., 123, 8172–8189, https://doi.org/10.1029/2017JD028169, 2018.

Mao, Z., Huang, K., Fang, J., Zhang, Z., Cao, R., and Yi, F.: An Observation of precipitation during cooling with Ka-Band cloud radar in Wuhan, China, Remote Sens.-Basel, 15, 5397, https://doi.org/10.3390/rs15225397, 2023.

Martucci, G., R. Matthey, V. Mitev, and H. Richner: Comparison between backscatter lidar and radiosonde measurements of the diurnal and nocturnal stratification in the lower troposphere, J. Atmos. Ocean. Tech., 24, 1231–1244, https://doi.org/10.1175/JTECH2036.1, 2007.

Moran, K. P., Martner, B. E., Post, M. J., Kropfli, R. A., Welsh, D. C., and Widener, K. B.: An unattended cloud-profiling radar for use in climate research, B. Am. Meteorol. Soc., 79, 443–455, https://doi.org/10.1175/1520-0477(1998)079<0443:AUCPRF>2.0.CO;2, 1998.

Neggers, R. A. J., Siebesma, A. P., Lenderink, G., and Holtslag, A. A. M.: An evaluation of mass flux closures for diurnal cycles of shallow cumulus, Mon. Weather Rev., 132, 2525–2538, https://doi.org/10.1175/MWR2776.1, 2004.

Pal, S., Behrendt, A., and Wulfmeyer, V.: Elastic-backscatter-lidar-based characterization of the convective boundary layer and investigation of related statistics, Ann. Geophys.-Italy, 28, 825–847,

https://doi.org/10.5194/egusphere-2024-933
Preprint. Discussion started: 2 May 2024

https://doi.org/10.5194/angeo-28-825-2010, 2010.

Pal, S., Lopez, M., Schmidt, M., Ramonet, M., Gibert, F., Xueref-Remy, I., and Ciais, P.: Investigation of the atmospheric boundary layer depth variability and its impact on the 222 Rn concentration at a rural site in France, J. Geophys. Res.-Atmos., 120, 623–643, https://doi.org/10.1002/2014JD022322, 2015.

Pearson, G., Davies, F., and Collier, C.: Remote sensing of the tropical rain forest boundary layer using pulsed Doppler lidar, Atmos. Chem. Phys., 10, 5891–5901, https://doi.org/10.5194/acp-10-5891-2010, 2010.

Piironen, A. K. and Eloranta, E. W.: Convective boundary layer mean depths and cloud geometrical properties obtained from volume imaging lidar data, J. Geophys. Res.-Atmos., 100, 25569–25576, https://doi.org/10.1029/94JD02604, 1995.

Ribeiro, F. N. D., Oliveira, A. P. D., Soares, J., Miranda, R. M. D., Barlage, M., and Chen, F.: Effect of sea breeze propagation on the urban boundary layer of the metropolitan region of Sao Paulo, Brazil, Atmos. Res., 214, 174–188, https://doi.org/10.1016/j.atmosres.2018.07.015, 2018.

Sandeep, A., Rao, T. N., Ramkiran, C. N., and Rao, S. V. B.: Differences in atmospheric boundary-layer characteristics between wet and dry episodes of the Indian summer monsoon, Bound.-Lay. Meteorol., 153, 217–236, https://doi.org/10.1007/s10546-014-9945-z, 2014.

Schneider, S. P.: Effects of roughness on hypersonic boundary-layer transition, J. Spacecraft Rockets, 45, 193–209, https://doi.org/10.2514/1.29713, 2008.

Schween, J. H., Hirsikko, A., Löhnert, U., and Crewell, S.: Mixing-layer height retrieval with ceilometer and Doppler lidar: from case studies to long-term assessment, Atmos. Meas. Tech., 7, 3685–3704, https://doi.org/10.5194/amt-7-3685-2014, 2014.

Seibert, P.: Review and intercomparison of operational methods for the determination of the mixing height, Atmos. Environ., 34, 1001–1027, https://doi.org/10.1016/S1352-2310(99)00349-0, 2000.

https://doi.org/10.5194/egusphere-2024-933
Preprint. Discussion started: 2 May 2024

Seidel, D. J., Ao, C. O., and Li, K.: Estimating climatological planetary boundary layer heights from radiosonde observations: Comparison of methods and uncertainty analysis, J. Geophys. Res.-Atmos., 115, 2009JD013680, https://doi.org/10.1029/2009JD013680, 2010.

Seidel, D. J., Zhang, Y., Beljaars, A., Golaz, J., Jacobson, A. R., and Medeiros, B.: Climatology of the planetary boundary layer over the continental United States and Europe, J. Geophys. Res.-Atmos., 117, 2012JD018143, https://doi.org/10.1029/2012JD018143, 2012.

Singh, N., Solanki, R., Ojha, N., Janssen, R. H. H., Pozzer, A., and Dhaka, S. K.: Boundary layer evolution over the central Himalayas from radio wind profiler and model simulations, Atmos. Chem. Phys., 16, 10559–10572, https://doi.org/10.5194/acp-16-10559-2016, 2016.

Solanki, R., Guo, J., Li, J., Singh, N., Guo, X., Han, Y., Lv, Y., Zhang, J., and Liu, B.: Atmospheric-boundary-layer-height variation over mountainous and urban sites in Beijing as derived from radar wind-profiler measurements, Bound.-Lay. Meteorol., 181, 125–144, https://doi.org/10.1007/s10546-021-00639-9, 2021.

Stull, R. B.: An Introduction to Boundary Layer Meteorology, Springer Netherlands, Dordrecht, https://doi.org/10.1007/978-94-009-3027-8, 1988.

Su, T., Li, Z., and Kahn, R.: A new method to retrieve the diurnal variability of planetary boundary layer height from lidar under different thermodynamic stability conditions, Remote Sens.-Basel Environ., 237, 111519, https://doi.org/10.1016/j.rse.2019.111519, 2020.

Tang, G., Zhang, J., Zhu, X., Song, T., Münkel, C., Hu, B., Schäfer, K., Liu, Z., Zhang, J., Wang, L., Xin, J., Suppan, P., and Wang, Y.: Mixing layer height and its implications for air pollution over Beijing, China, Atmos. Chem. Phys., 16, 2459–2475, https://doi.org/10.5194/acp-16-2459-2016, 2016.

Tennekes, H. and Driedonks, A. G. M.: Basic entrainment equations for the atmospheric boundary layer, Bound.-Lay. Meteorol., 20, 515–531, https://doi.org/10.1007/BF00122299, 1981.

Träumner, K., Kottmeier, C., Corsmeier, U., and Wieser, A.: Convective boundary-layer entrainment: short review and progress using doppler lidar, Bound.-Lay. Meteorol., 141, 369–391, https://doi.org/10.1007/s10546-011-9657-6, 2011.

Tucker, S. C., Senff, C. J., Weickmann, A. M., Brewer, W. A., Banta, R. M., Sandberg, S. P., Law, D. C., and Hardesty, R. M.: Doppler lidar estimation of mixing height using turbulence, shear, and aerosol profiles, J. Atmos. Ocean. Tech., 26, 673–688, https://doi.org/10.1175/2008JTECHA1157.1, 2009.

Van Der Kamp, D. and McKendry, I.: Diurnal and seasonal trends in convective mixed-layer heights estimated from two years of continuous ceilometer observations in Vancouver, BC, Bound.-Lay. Meteorol., 137, 459–475, https://doi.org/10.1007/s10546-010-9535-7, 2010.

Yang, T., Wang, Z., Zhang, W., Gbaguidi, A., Sugimoto, N., Wang, X., Matsui, I., and Sun, Y.: Technical note: Boundary layer height determination from lidar for improving air pollution episode modeling: development of new algorithm and evaluation, Atmos. Chem. Phys., 17, 6215–6225, https://doi.org/10.5194/acp-17-6215-2017, 2017.

Yates, D. N., Chen, F., Lemone, M. A., Qualls, R., Oncley, S. P., and Gross, R. L.: A cooperative atmosphere-surface exchange study (CASES) dataset for analyzing and parameterizing the effects of land surface heterogeneity on area-averaged surface heat fluxes, J. Appl. Meteorol., 40, https://doi.org/10.1175/1520-0450(2001)040<0921:ACASES>2.0.CO;2, 2001.

Zhang, J., Guo, J., Li, J., Zhang, S., Tong, B., Shao, J., Li, H., Zhang, Y., Cao, L., Zhai, P., Xu, X., and Wang, M.: A Climatology of merged daytime planetary boundary layer height over China from radiosonde measurements, J. Geophys. Res.-Atmos., 127, e2021JD036367, https://doi.org/10.1029/2021JD036367, 2022.

Zhang, M., Tian, P., Zeng, H., Wang, L., Liang, J., Cao, X., and Zhang, L.: A comparison of wintertime atmospheric boundary layer heights determined by tethered balloon soundings and lidar at the site of

https://doi.org/10.5194/egusphere-2024-933
Preprint. Discussion started: 2 May 2024

SACOL, Remote Sens.-Basel, 13, 1781, https://doi.org/10.3390/rs13091781, 2021.

Zhang, Y., Zhang, S., Huang, C., Huang, K., Gong, Y., and Gan, Q.: Diurnal variations of the planetary boundary layer height estimated from intensive radiosonde observations over Yichang, China, Sci. China Technol. Sc., 57, 2172–2176, https://doi.org/10.1007/s11431-014-5639-5, 2014.

https://doi.org/10.5194/egusphere-2024-933
Preprint. Discussion started: 2 May 2024

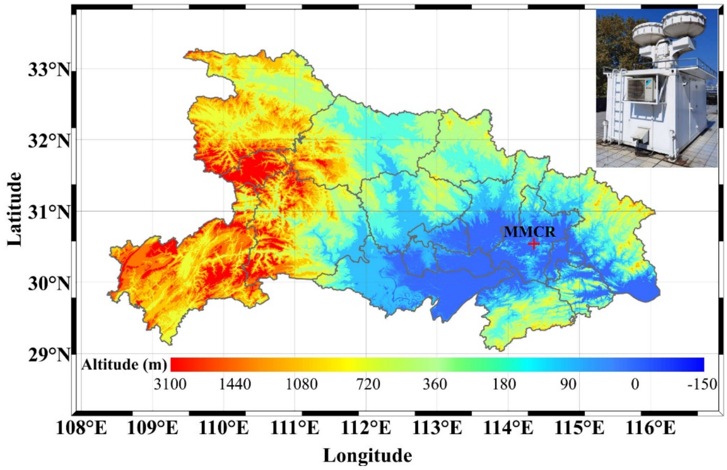

Figure 1. Topographic elevation map of Hubei Province and Ka-band MMCR located in Wuhan University (30.54°N, 114.36°E). The red crisscross denotes the site of MMCR.

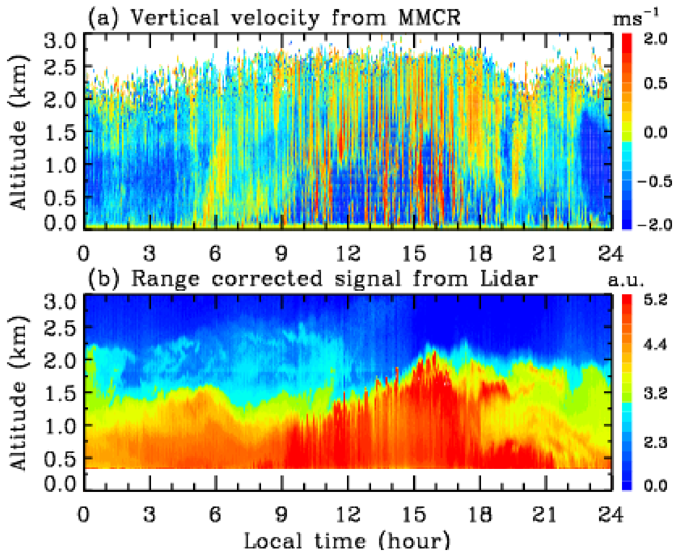

Figure 2. Time-height section of (a) vertical velocity from MMCR and (b) RCS from lidar on 15 August 2020.

https://doi.org/10.5194/egusphere-2024-933
Preprint. Discussion started: 2 May 2024

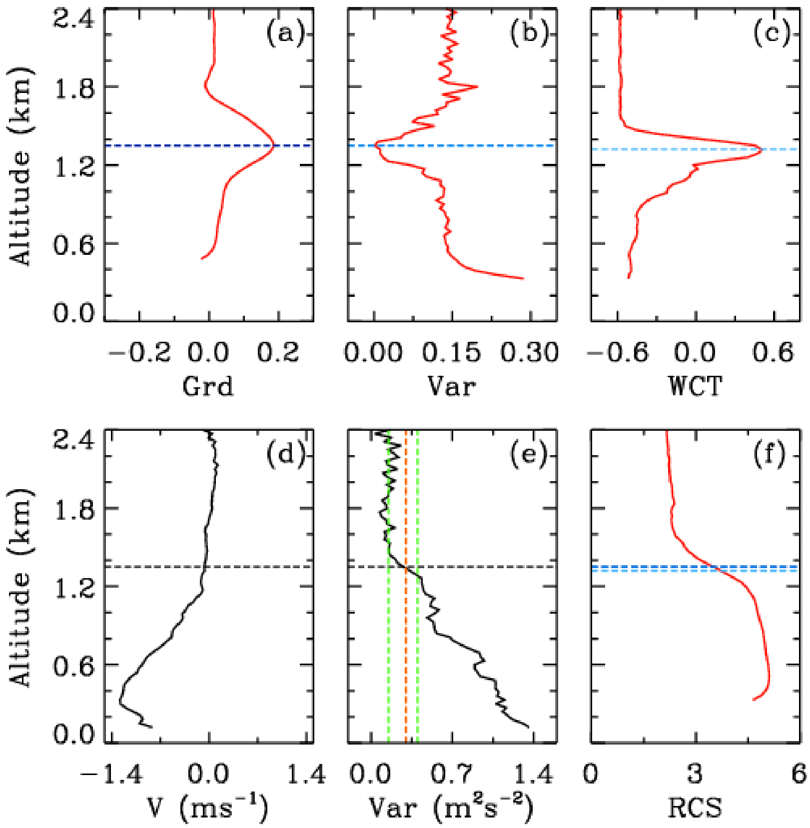

Figure 3. Profiles of (a) RCS gradient, (b) variance, (c) WCT and (f) RCS form lidar, and (e) vertical velocity and (g) its variance from MMCR between 12:15 and 12:45 LT on 15 August 2020. In these panels, the horizontal lines in different colors represent the CBLH determined by different methods. In Panel 3e, the orange vertical line denotes the selected threshold of 0.3 $m^2 s^{-2}$, and the two green vertical lines correspond to the variances of 0.15 and 0.4 $m^2 s^{-2}$, respectively.

https://doi.org/10.5194/egusphere-2024-933
Preprint. Discussion started: 2 May 2024

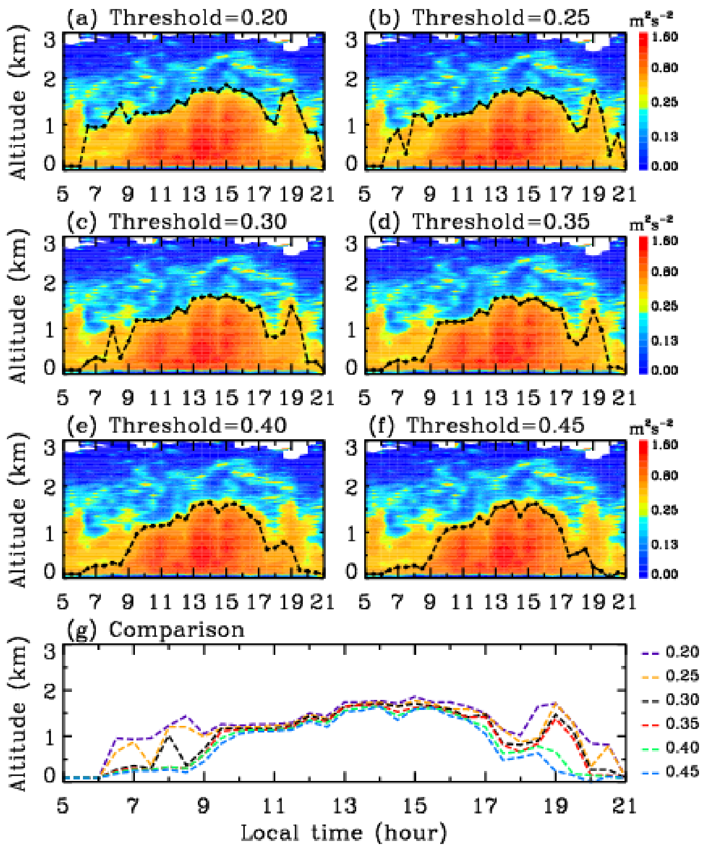

Figure 4. CBLHs derived from thresholds of (a) 0.2, (b) 0.25, (c) 0.3, (d) 0.35, (e) 0.4 and (f) 0.45 $m^2 s^{-2}$ superimposed over vertical velocity variance (color shading) from MMCR on 15 August 2020, and (g) their comparison.

https://doi.org/10.5194/egusphere-2024-933
Preprint. Discussion started: 2 May 2024

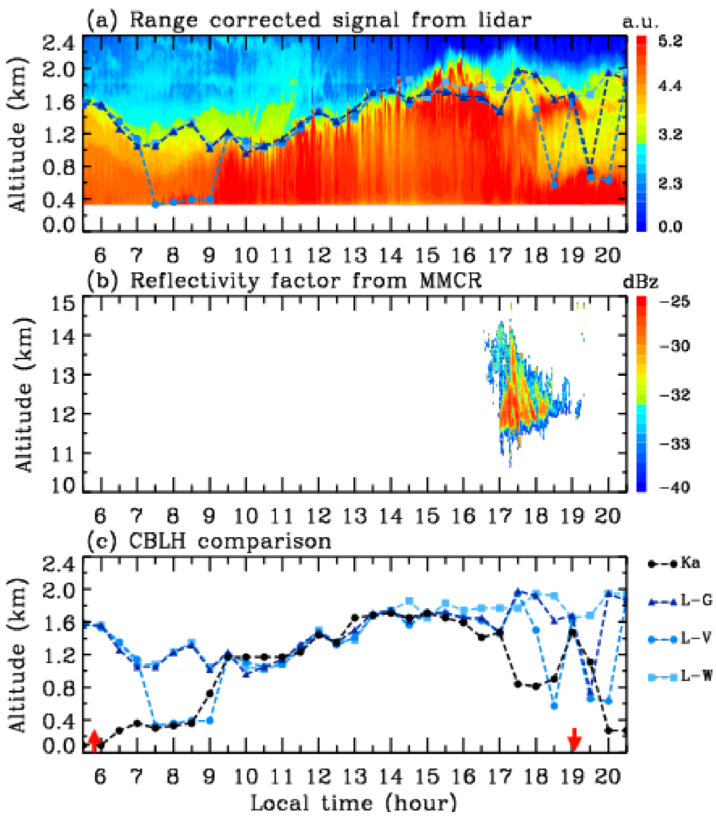

Figure 5. (a) Evolution of CBLH derived from RCS gradient, variance and WCT superimposed over lidar RCS (color shading) on 15 August 2020, (b) reflectivity factor from MMCR, and (c) comparison of CBLHs derived from MMCR and lidar observations. The black dash curve with circle (Ka) denotes the CBLH determined by the variance threshold of 0.3 $m^2 s^{-2}$ in the Ka-band MMCR observation, while the dark blue, blue and light blue dash curves with triangle (L-G), circle (L-V) and square (L-W) represent the CBLH determined by the gradient, variance and WCT in the lidar measurement, respectively. In Panel 5c, the two red arrows denote the time of sunrise and sunset at 05:50 and 19:05, respectively.

https://doi.org/10.5194/egusphere-2024-933
Preprint. Discussion started: 2 May 2024

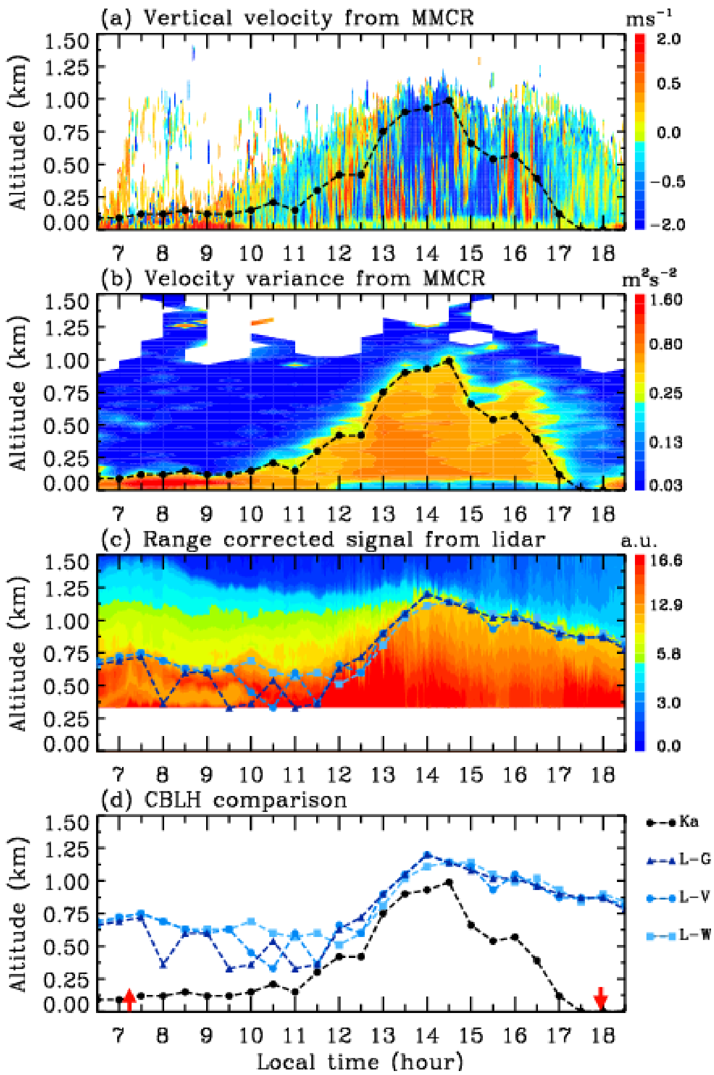

Figure 6. Distributions of (a) vertical velocity and (b) its variance from MMCR and (c) lidar RCS on 31 January 2020 with retrieved CBLH, and (d) comparison of CBLHs derived from MMCR and lidar observations. The threshold of vertical velocity variance from the MMCR is 0.3 $m^2 s^{-2}$. In Panel 6d, the two red arrows denote the time of sunrise and sunset at 07:15 and 17:57, respectively.

https://doi.org/10.5194/egusphere-2024-933
Preprint. Discussion started: 2 May 2024

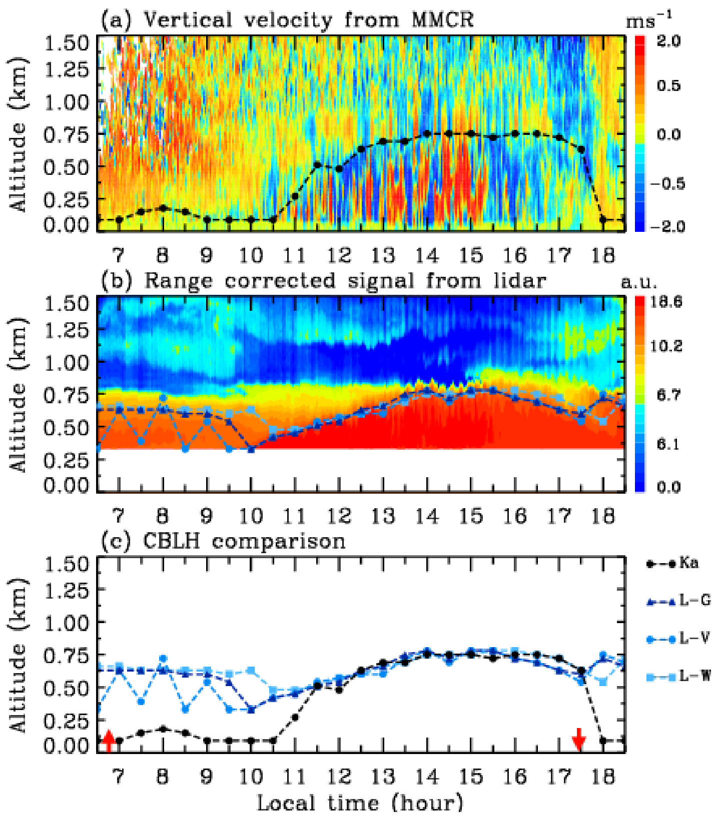

Figure 7. Distributions of (a) vertical velocity from MMCR and (b) lidar RCS on 12 November 2020 with retrieved CBLH, and (c) comparison of CBLHs derived from MMCR and lidar observations. The threshold of vertical velocity variance from the MMCR is 0.3 $m^2 s^{-2}$. In Panel 7c, the two red arrows denote the time of sunrise and sunset at 06:47 and 17:27, respectively.

https://doi.org/10.5194/egusphere-2024-933
Preprint. Discussion started: 2 May 2024

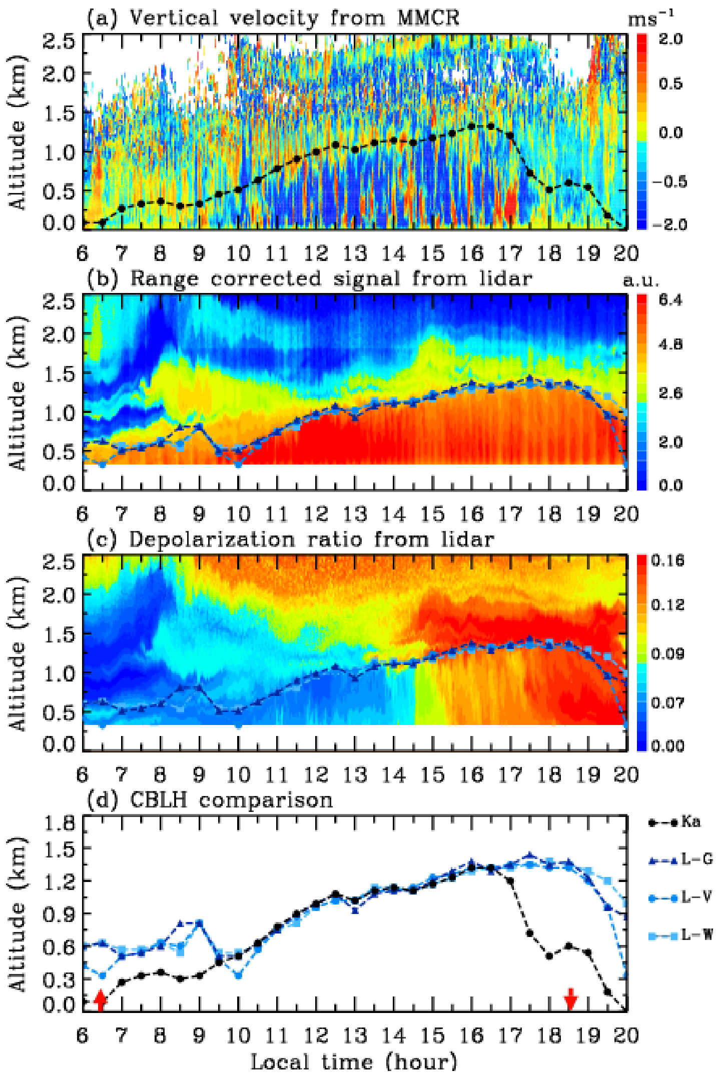

Figure 8. Distributions of (a) vertical velocity from MMCR and lidar (b) RCS and (c) depolarization ratio on 19 March 2020 with retrieved CBLH, and (d) comparison of CBLHs derived from MMCR and lidar observations. The threshold of vertical velocity variance from the MMCR is 0.3 $m^2 s^{-2}$. In Panel 8d, the two red arrows denote the time of sunrise and sunset at 06:27 and 18:34, respectively.

https://doi.org/10.5194/egusphere-2024-933
Preprint. Discussion started: 2 May 2024

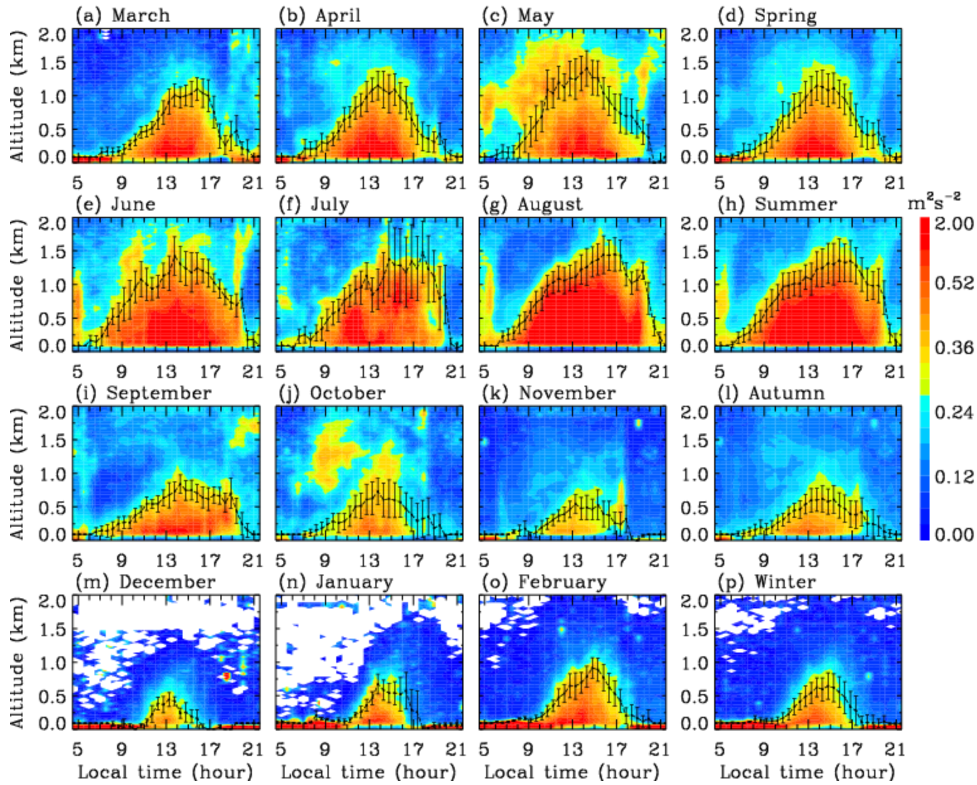

Figure 9. Monthly and seasonal mean values and statistical standard deviations of CBLH estimated by threshold of vertical velocity variance from MMCR. The variance threshold is 0.3 $m^2 s^{-2}$, and the color shading denotes the variance distribution. The months and seasons are marked above the corresponding panels, respectively.

https://doi.org/10.5194/egusphere-2024-933
Preprint. Discussion started: 2 May 2024

713
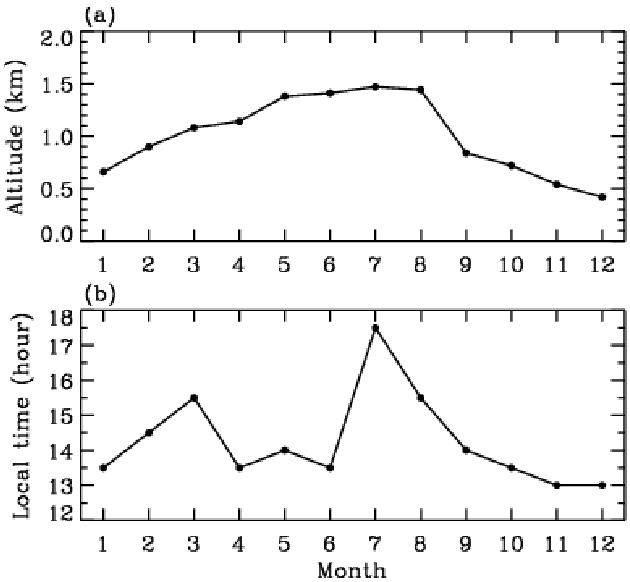

714 **Figure 10.** (a) Maximum value and (b) occurrence time of monthly mean CBLH derived from threshold of

715 vertical velocity variance in MMCR observation.

https://doi.org/10.5194/egusphere-2024-933
Preprint. Discussion started: 2 May 2024

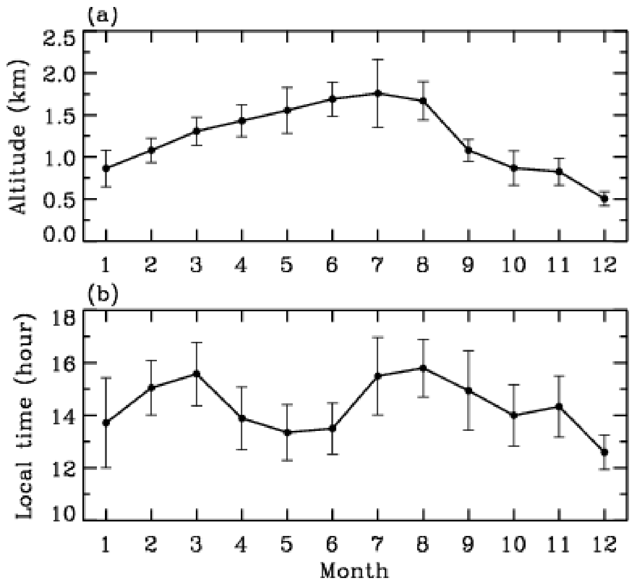

Figure 11. Monthly mean values and statistical standard deviations of (a) daily maximum CBLH and (b) its occurrence time derived from threshold of vertical velocity variance in MMCR observation.